Predicted ripple dimensions in relation to the precision of in situ measurements

Knut Krämer[1] and Christian Winter[1]

[1]MARUM - Center for Marine Environmental Sciences, University of Bremen, Leobener Str., D-28359 Bremen, Germany

Correspondence to: Knut Krämer (kkraemer@marum.de)

Abstract. Ripples are common morphological features in sandy marine environments. Their shapes and dimensions are closely related to local sediment properties and the forcing by waves and currents. Numerous predictors for the geometry and hydraulic roughness of ripples exist but due to their empirical nature, they may fail to properly reflect conditions in the field. Here, situ measurements of ripple dimensions and their dynamics in a shallow shelf sea are reported. Technical and methodological limits of the detection of ripple dimensions and their dynamic evolution due to changing forcing are assessed. Methods of bed detection from sonar data and analysis of ripple dimensions in digital elevation models (DEM) are compared and evaluated. The range of measured ripple dimensions is quantified and compared to results of traditional and recent empirical predictors. The precision of measurements of bedform dimensions is taken as the repeatability of a measurement for inactive conditions and the accuracy of measurement is assessed via comparison to predicted dimensions. The precision of detection is limited to 10% of the absolute ripple dimensions. The order of magnitude of the ripple dimension can be predicted by the empirical relations. However, these tend to return the height of the largest ripples rather than average heights. The application of different methods for detection of heights may result in derived form roughness heights by up to a factor of two.

1 Introduction

Small scale bedforms like ripples are ubiquitous morphological features in sandy coastal and shelf sea environments. Their formation and dynamics are controlled by waves and currents, while their equilibrium dimensions are commonly described to be related to a characteristic sediment grain size. The existence and evolution of ripples play important roles in the interaction between sea bed and water column (Grant and Madsen, 1979; Bartholdy et al., 2015). Hydraulic roughness and extraction of momentum from the mean flow is enhanced beyond the effect of mere grain roughness by several orders of magnitude due to the presence of ripples (Zanke, 1982; Soulsby, 1997). Furthermore, the presence of ripples influences turnover rates of nutrients and pollutants in the benthic environment when compared to a flat seabed (Nelson et al., 2013; Ahmerkamp et al., 2015).

If the threshold of motion, expressed as critical bed shear stress or dimensionless Shields parameter, for a characteristic grain size is exceeded, sediment is transported and bedforms develop. Recent equilibrium ripple predictors based on extensive laboratory and field datasets exist for waves (e.g. Soulsby et al., 2012; Nelson et al., 2013), currents (e.g. Soulsby et al., 2012; Bartholdy et al., 2015) or for combined flows (e.g. Li and Amos, 1998). A classification of the type of bedform and corresponding dominant forcing can be made using the ratio of wave and current shear stress. Wave ripples can be subdivided

into orbital ripples scaling with wave orbital diameter (Traykovski et al., 1999), anorbital ripples scaling with grain size (Maier and Hay, 2009) and intermediate forms (Clifton and Dingler, 1984). The dimensions of current ripples are usually related to grain size only (Yalin, 1964, 1985). In contrast to dunes, ripple dimensions are described as independent of the flow depth (see classification in Venditti, 2013) although Bartholdy et al. (2015) do include flow depth in a limited range using a virtual
5 boundary layer concept.

Under nonsteady forcing conditions, bedforms continuously adjust in shape and eventually migrate. Equilibrium ripple predictors may not capture this adaptation process resulting in poor prediction of ripple dimensions during active periods. Time-evolving (nonsteady) ripple predictors have only recently been suggested by Traykovski (2007) and Soulsby et al. (2012). These models use an exponential relaxation with a given timescale and rate-of-change coefficients during active conditions to
10 allow for smooth transitions of bedform dimensions and also include decay processes due to wash-out and sheet flow based on additional critical shear stress levels as well as bioturbation.

While a large number of empirical ripple predictors has been derived from data acquired in flume studies, the interaction between physical and biological processes in the field is not yet fundamentally understood. Hydrodynamic boundary conditions, local sedimentology and (micro-)biological effects in the field may be different from flume experiments, e.g. in combined
15 current and waves, in tidal environments dominated by periodically changing flow conditions, or in deep sea environments. This makes field data a necessary prerequisite for the understanding, modeling, assessment of bed conditions (Schindler et al., 2015; Malarkey et al., 2015).

Methods of ripple measurements in laboratory flumes and in the field make use of optical and acoustical instrumentation. Among others, Li and Amos (1998) used underwater cameras in combination with a scale bar to determine ripple wave lengths.
20 Hay and Wilson (1994) and later Hay and Mudge (2005) used rotary side scan sonar images to describe the evolution of bedform wave lengths during storms. Traykovski (2007) used a sector scanning sonar to measure ripple wave lengths while estimating the height of migrating ripples from the time series of a local bed level from an acoustic backscatter sensor. Bell and Thorne (2007) developed a 3D profiling sonar enabling them to measure the small scale bathymetry of rippled sea beds. Before that, the same authors deployed a 2D scanning sonar to measure ripple dimensions along transects (Bell and Thorne, 1997). Janssen
25 (2004) collected high resolution bathymetry data using a laser line in rectified camera images taken from a moving sledge.

Commonly, spatially averaged values of ripple properties are given while the ranges and the statistical distribution are often not reported. However, van der Mark et al. (2008) show that even in laboratory experiments with uniform sediment and stationary flow conditions, bedforms are far from regular features.

Understanding of the dynamics of in situ ripple fields may be impeded by relict ripples, which are observed under conditions
30 unrelated to their formation. These may be inactive bedforms during low flow conditions (around slack water in tidal environments, or after a storm), which may additionally decay through bioturbation i.e., the activity of benthic and demersal fish or burrowing marine organisms (Amos et al., 1988; Soulsby et al., 2012). When measuring ripples in field conditions for short periods on tidal cycle time scales, their dimensions will most likely not be in equilibrium with the present forcing conditions. If ripples are actively evolving, their shapes and dimensions adapt towards a new equilibrium with the instantaneous forcing.
35 Furthermore, their dimensions and shape can change drastically, when the nature of the dominant forcing changes from strong

wave to current dominance or vice versa (Amos and Collins, 1978). This paper is focused on active ripples i.e., bed conditions in which the shape or dimensions of ripples change over the observation time frame or in which they migrate without changing their general shape or orientation.

In a field campaign, hydro- and morphodynamic data on the forcing and ripple characteristics have been collected within tidal

5 cycles on a sandy shelf seabed in the North Sea. The measurement setup and the devices used are described. The ranges and error margins determined by the technical specifications of the sensors and different methods employed to derive parameters from raw sensor data are reported. The influence of the methods on the detected range of bedform dimensions is evaluated and the measured dimensions are compared to values predicted for wave and current ripples. Implications for the calculation of bedform roughness from ripple dimensions are discussed.

10 ## 2 Methods

2.1 Study site

Field data was acquired during cruises on RV *Heincke* to the German Bight at station D (54.09118° N, 7.35881° E) of the NOAH[1] project (North Sea Observation and Assessment of Habitats). An autonomous lander was deployed for periods longer than 25 hours to cover the diurnal inequality in the tidal cycle. The data discussed here was obtained during cruise HE441

15 (20–28 March 2015) over a period of around 36 hours. The station was also visited during cruise HE447 in June 2015 (Fig. 1) but the bedforms were inactive.

Station NOAH-D is located in a water depth of 35 m. A survey of the area surrounding the deployment site by multibeam echosounder revealed a flat and featureless bathymetry on the larger scale. The grain size analysis of grab samples taken prior to deployment of the lander showed bed sediment consisting of fine sand with a median grain size $d_{50} = 105$ µm.

20 ### 2.2 Lander deployments

Intra-tidal hydro- and morphodynamics are observed by the autonomous seafloor observatory *SedObs* (Fig. 1a). The lander was developed for the COSYNA[2] initiative (Coastal Observing System for Northern and Arctic Seas). The lander consists of a steel frame with a 2×2 m grating platform providing space for battery power supply and the installation of sensors. The platform rests on four slim height-adjustable inclined legs to which further sensors can be attached closer to the sea

25 bed. Weighted foot plates provide stable stand, prohibit subsidence and reduce scouring around the legs. For the application described here, the measurement platform was located approximately 2 m above the sea floor to minimize distortions of the near-bed velocity profile. The instrumentation comprises optical and acoustic sensors for the measurement of hydrodynamics, small scale bathymetry and environmental conditions. The lander is deployed from shipboard with the help of a launching frame for positioning in relation to tidal flow direction and is recovered by acoustic release of floating buoys.

---

[1] www.noah-project.de

[2] www.hzg.de/institutes_platforms/cosyna/index.php.en

2.3 Devices and data

The devices used in this study are summarized in Tab. 1. An acoustic Doppler current profiler (ADCP; Teledyne RDI Workhorse Rio Grande 1200 kHz) was used to record the near-bed velocity profile below the lander. The along-beam resolution of the downward-looking ADCP was 0.1 m and the instrument sampled at a frequency of 1 Hz. Additionally, two Acoustic Doppler Velocimeters (ADVs; Nortek Vector) recorded point-wise velocity data at two levels (0.12 m and 0.45 m above seabed) with a sampling frequency of 32 Hz. In combination with the pressure signal recorded in their housings, the velocity data can be used to calculate wave paramaters.

The small scale bathymetry below the lander was recorded by means of a 1 MHz 3D acoustic ripple profiler (3D-ARP; Marine Electronics Ltd. (2004); Bell and Thorne (2007)). Its pencil-beam sonar transducer with an effective beam width of 1.8° is mounted on a rotating and tilting mechanism in an oil-filled pressure housing. In a stepwise procedure, the sonar is tilted through a preset arc in 0.9° steps, recording along-beam echo intensities from the water column for every ping. After completing one swath, the transducer is rotated by 0.9° about the vertical axis and tilted to the arc starting angle to record the next swath (see Fig. 2a for definition of terms). For our applications, the swath arc was limited to 120° because for grazing angles $\gamma < 30°$ the energy backscattered to the sonar transducer rapidly decreases and the bed echo cannot be detected reliably against background noise. With the sensor installed 1.8 m above the seafloor, a circular area of 6.2 m diameter was covered by the scans. In our setup, a full bathymetry scan was recorded every 12 minutes. The raw echo intensity data was stored in camera raw format (rw2) with an ASCII header containing sensor settings and environmental parameters and a binary data section listing echo intensity values of successive samples, pings and swaths.

Sediment properties were determined from Shipek grab samples taken at the investigated site before lander deployment. Grain size distribution and statistical parameters derived hereof such as median grain size d_{50} were analyzed by means of a laser diffraction particle size analyzer (Beckman Coulter).

2.4 Bed detection methods

The raw 3D-ARP data is available as a three-dimensional matrix $\mathbf{S}^{i \times j \times k}$, containing the echo intensities for the number of i samples along the beam, j pings along a swath and k swaths of a full scan. The general form of the echo recorded in individual pings exhibits a high echo level close to the sonar transducer due to ringing. This part of the signal within the near range of the sonar is blanked before further processing. With increasing range from the transducer, the backscattered echo level declines due to signal losses to reverberation and scattering in the water column. Near the bed range, a steep increase to a maximum level can be observed, followed by a more gentle decline towards a constant background noise level. Averaged echo shapes for variable grazing angles are illustrated in Fig. 3.

To reduce noise, the raw echo signals are smoothed by a five-point moving average in along-beam direction. The resulting echo intensity profiles are evaluated for the maximum echo, as the bed usually contributes the strongest reflector. The simplest method of bed detection is therefore to pick the maximum echo in the smoothed ping data. However, as marine life or other

instrumentation in the sonar beam may also contribute strong reflectors, the water column echo was only evaluated within a certain depth range around the expected bed level.

Threshold level methods for bed picking from similar sonar data were used by Smyth and Li (2005) and by Lefebvre (2009), who detect the bed at the level l_p where $l_p \geq 0.6\,l_{max}$ or $l_p \geq 0.8\,l_{max}$ of the maximum ping-wise echo level l_{max} is exceeded,

5 respectively. These approaches are extended to account for the widening of the along-beam target shape with grazing angles increasing outward from nadir where the sonar footprint is ensonified over a growing period of time (see Fig. 3). Therefore, a threshold level as a function of the grazing angle is introduced:

$$l_p = \left[1 - \sqrt{(\cos\gamma)}\right] l_{max} \tag{1}$$

with values ranging from $l_p = 0.7$ at the outer swath beams to $l_p = 1.0$ at the nadir beam.

10 Apart from the threshold level, further methods using the first and second along-beam derivatives of the echo intensity, echo gradient and echo curvature were tested. The maximum echo gradient is usually found midway between background noise level and maximum echo intensity in the rising slope of the bed echo, given that it is resolved by a sufficient number of samples. The maximum in echo curvature represents the onset of the rising slope.

The last approach for bed detection tested is the cross-correlation with an idealized bed echo model. The bed level in a single

15 water column ping is then found at the along-beam range where the cross-correlation of the recorded ping echo and the echo model is maximized. Bell and Thorne (1997) designed a model of the bed echo (target) represented by a sine wave accounting for the acoustic pulse length and the incident angle between sonar lobe and seabed. The model echo is cross-correlated with the echo profiles and the index of maximum correlation denoting the best fit between echo model data is converted to bed range. To account for variable environmental conditions, for every scan 200 samples (180° in 0.9° steps) of echoes for every grazing

20 angle can be taken into account. Averaging the individual pings over all swath angles, a data derived echo model without the need to design an idealized echo shape is obtained.

2.5 Coordinate conversion and gridding

The beam coordinates of the detected bed level are computed considering the sound velocity and two-way travel time of the sonar signal yielding an along-beam range. Together with the tilt and rotation angles for the corresponding ping and swath, the

25 bed level is described in spherical coordinates (r, θ, φ) which are in turn transferred to Cartesian coordinates (x, y, z).

The along-beam resolution can be estimated from the overall beam range and the number of samples. Typical settings are a beam range of $r_{max} = 4$ m and $n_i = 889$ samples; the resulting vertical resolution for the central vertical beam (nadir) is $\Delta_z = 0.0045$ m. The horizontal resolution is controlled by the area of the sonar footprint as well as tilt and rotation steps. With a beam angle of $\beta = 1.8°$ (±3 dB points conical, Marine Electronics Ltd. (2004)) and a sonar height of $h_s = 1.8$ m above the

30 seabed, the nadir beam ensonifies a circular area of $w_f = 0.056$ m diameter. At the maximum grazing angle $\gamma_{max} = 60°$, the total area ensonified over the echo pulse length has a width $w_f = 0.226$ m in the swath plane. The beam spacing is set to 0.9° steps, resulting in an along-swath spacing of $\Delta s = 0.028$ m at nadir ($\gamma = 0°$), $\Delta s = 57$ mm at $\gamma = 45°$ and $\Delta s = 0.116$ m at the maximum grazing angle. The local bathymetry in the area of the sonar footprint is thus possibly underestimated at the depth of

troughs and the height of crests (see Fig. 2b). Assuming a triangular crest shape and a maximum ripple slope equal to the angle of repose of sand $\alpha = 32°$, the maximum error in underestimating ripple crest heights yields $\varepsilon_{max} = 0.25 \cdot w_f \cdot \tan \alpha = 0.009$ m at nadir and $\varepsilon_{max} = 0.035$ m at the outermost beam in our configuration. As ripple troughs are usually more flat, the error for and underestimation of through depths is expected to be less pronounced. With a typical aspect ratio $\psi = \eta/\lambda = 0.1$ much

5   lower than the angle of repose, the maximum error reduces to $\varepsilon_{max} = 0.125 \cdot w_f \cdot \psi = 0.001$ m at nadir.

For comparability among successive scans, the scattered data points are gridded with a horizontal resolution of $\Delta x = \Delta y = 0.025$ m resulting in digital elevation models (DEM) with consistent grid cells.

In the last processing step, the bathymetry is cropped to the central area of 2 m by 2 m for further evaluation of bedform characteristics. This limitation is made because the area outward of the lander legs is shadowed from the sonars field of view

10   and scouring may influence the area in vicinity of the feet. Additionally, the maximum grazing angle for the cropped area is limited to $\gamma = 30°$, reducing the effects of increasing beam spacing and sonar footprint. To better distinguish local ripple features, the global trend of the larger scale surrounding bathymetry is computed from the average bathymetry of all scans of a deployment and removed. The resulting residual zero-mean bathymetry is evaluated by the following methods.

2.6   Ripple geometry

15   Ripple geometry can be described by the orientation of crests lines in the horizontal plane φ and the cross-sectional dimensions; height η, wave length λ and aspect ratio $\psi = \eta/\lambda$. The dominant forcing can be distinguished from ripple cross-sectional shape: In contrast to symmetric wave ripples, current ripples exhibit a steeper downstream (lee) slope and a more gently inclined upstream (stoss) slope. A classification for a number of transitional forms between pure wave and current ripples is given by Amos et al. (1988). The ratio of the stoss and lee slope lengths can be used to identify bedform orientation with regard to the

20   dominant forcing and indicate migration in this direction (Knaapen, 2005).

The geometry of the ripples is extracted from the gridded bathymetry datasets. First, the crest-transverse orientation θ of the ripple field is derived: The gridded datasets are transferred into binary image matrices using a threshold equal to half the standard deviation of the global elevation $z_{tr} = 0.5 \ \sigma_z$ (Fig. 2c). The binary images are processed using 8-connected neighborhoods to identify crest areas of individual bedforms. The detected objects are represented by ellipses of equal area.

25   Small and circular objects are removed by means of minimum area and ratio of the ellipses semi-axes. The average orientation of the remaining objects is used as characteristic ripple orientation. Figure 4 shows an example for the cropped bathymetry, the binary image with detected ripple orientation and the corresponding distribution of crest-perpendicular orientation in the polar histogram. The precision in orientation detection throughout successive scans, even for inactive bedforms is in the order of $10°$. To avoid abrupt changes in the subsequent computation of bedform height and length, the ensemble average ripple orientation

30   is computed for every deployment, given that it does not change significantly over time. Afterwards, the scans are rotated using the average ripple orientation and re-interpolated to the original Cartesian grid for extraction of ripple dimensions using the following three methods:

1. Statistical method ($\eta_{m,s}$)

2. Image extrema method ($\eta_{m,i}$)

3. Transect method ($\eta_{m,t}$, $\lambda_{m,t}$)

The first is a statistical estimate using the distribution of bed elevations. The standard deviation of elevation, multiplied by a factor $k = 2\sqrt{2}$ was used to estimate bedform heights η_s by Traykovski et al. (1999) and Smyth and Hay (2002). This method
5 is usually employed to compute root mean square wave height from water level records and assumes sinusoidal bedform cross sections.

The second method finds local extrema in the 3D bathymetry as grid cells surrounded by cells of lower (crest) or higher elevation (through), similar to finding extreme pixel values in raster images. The averaged ripple η_i height is computed from the range between crests and troughs.
10 For the third method, transect are defined perpendicular to the crest orientation and evaluated for local extrema (crest and trough) by zero up- and down-crossing. The computed bedform height η_t is the average range between maxima and minima. Apart from height, bedform length λ_t is also computed by the transect method as the average along-transect distance between two successive crests. With the DEM spacing and cropping window size used, a total of 80 transects of $2\,\mathrm{m}$ length are evaluated. The advantage of the transect method is that it captures a range of bedform dimensions and therefore yields not only average
15 values for the overall bathymetry but also a distribution of heights and lengths.

As an alternative, ripple orientation and length can also be determined from spectra obtained from the 2D discrete Fourier transform (DFT) of the gridded bathymetry (Traykovski, 2007; Lefebvre, 2009; Nelson and Voulgaris, 2014) or from 2D autocorrelation.

2.7 Predictors for ripple dimensions

20 A number of predictors for wave and current ripple geometry exists in literature. An overview and evaluation of the performance of wave ripple predictors with an extensive dataset from lab and field experiments can be found in Nelson et al. (2013). Soulsby and Whitehouse (2005) present a literature review of predictors for wave, current and combined ripples and Soulsby et al. (2012) recently developed a combined, time-evolving predictor. After determining the dominant forcing, two formulations for wave or current ripples are employed to determine equilibrium height which is then used in an exponential relaxation in the
25 time-stepping procedure (Soulsby et al., 2012).

The following ripple predictors are evaluated with the given grain size and hydrodynamic data and compared to measured dimensions. The traditional current ripple predictors of Yalin (1964, 1985) (Ya64, Ya85) for length and Flemming (1988) (Fl88) for ripple height were selected as they are widely used and the recent wave and current ripple predictors of Soulsby et al. (2012) (So12w, So12c) is used as it is applicable to mixed forcing conditions.

2.7.1 Current ripples

Current generated ripple dimensions are usually described as independent of hydrodynamic parameters but scaling with grain size and immersed weight only. An early work by Yalin (1964) which is still widely used predicts current ripple length as:

$$\lambda_c = 1000 \cdot d_{50} \tag{2}$$

and was later revised including additional data (Yalin, 1985) in the form:

$$600 \cdot d_{50} \leq \lambda_c \leq 2000 \cdot d_{50} \tag{3}$$

While the ratio between bedform height and length may be derived using an empirical relation with the best fit to a large dataset from laboratory and field data by Flemming (1988):

$$\eta_c = 0.0677 \cdot \lambda_c^{0.8098} \tag{4}$$

the maximum bedform height is defined by the same author as:

$$\eta_{c,\max} = 0.16 \cdot \lambda_c^{0.84} \tag{5}$$

Soulsby et al. (2012) predict maximum dimensions of current ripples as follows. For height they obtain:

$$\eta_{c,\max} = d_{50} \cdot 202 \cdot D_*^{-0.554} \tag{6}$$

and wave length yields:

$$\lambda_{c,\max} = d_{50} \cdot (500 + 1881 \cdot D_*^{-1.5}) \tag{7}$$

Equation (6) and Eq. (7) are a valid in a range of $1.2 < D_* < 16$, where D_* is the dimensionless grain size defined as:

$$D_* = \left[\frac{g(s-1)}{\nu^2} \right]^{1/3} d_{50} \tag{8}$$

with the density ratio of sediment and water $s = \rho_s/\rho_w$, gravitational acceleration g and kinematic viscosity of water ν. These maximum ripple dimensions are reduced during wash-out conditions and existing ripples are completely eliminated by sheet flow. The different flow regimes are delineated by respective critical Shields parameters. In the measurements presented here, supercritical Shields parameters for bed load transport were found but they remained far below wash-out and sheet flow conditions, thus only the maximum ripple dimensions are used here.

2.7.2 Wave ripples

Predicted wave ripple dimensions commonly scale with a dimensionless number derived from wave parameters in relation to sediment grain size and immersed weight. Soulsby et al. (2012) found that the use of the ratio of wave orbital amplitude

and median grain size $\Delta = A/d_{50}$ as independent variable gives the best representation of a large dataset of measured ripple dimensions from flume and field studies. They use the following empirical predictors for wave induced ripple wave length:

$$\lambda_w = \left[1 + 1.87 \times 10^{-3}\Delta(1 - \exp(-(2.0 \times 10^{-4}\Delta)^{1.5}))\right]^{-1} A \tag{9}$$

and height:

$$\eta_w = 0.15\left(1 - \exp(-(5000/\Delta)^{3.5})\right)\lambda_w \tag{10}$$

2.8 Hydraulic roughness

When bedform dimensions are known, their hydraulic roughness length can be obtained using empirical relations (Li and Amos, 1998; Lefebvre et al., 2011). The impact of form roughness due to bedforms is important for numerical models as is exceeds the effect of grain roughness k_g by two orders of magnitude (e.g. Soulsby, 1997). A widely used (bed-)form roughness predictor is defined by van Rijn (1984):

$$k_{s,f} = 1.1 \cdot \eta \cdot (1 - e^{-25\eta/\lambda}) \tag{11}$$

Another common form of roughness length derived from ripple dimensions is $k_f = f(\eta^2/\lambda)$ with height in a power of two over length (see list in Lefebvre et al., 2011) with varying scaling scaling factors. Soulsby (1997) presents it as follows:

$$z_{0,f} = a_r \frac{\eta^2}{\lambda} \text{ (with scaling factor typically } a_r = 1). \tag{12}$$

3 Results

3.1 Bed detection

An inter-comparison of the different methods for bed detection shows that all threshold level methods reproduce the characteristics of the rippled seabed (Fig. 5). They mainly differ in the absolute level of average depth. The maximum echo gradient, maximum echo curvature and 60% maximum echo method (Smyth and Li, 2005) provide a median depth around 0.025 m higher than the median depth computed by the remaining methods. Additionally, the 60% max. method exhibits a slight dependence on the grazing angle and returns a bowl-shaped bathymetry (see Fig. 5b). The comparison of the different bed detection methods revealed that picking the maximum amplitude of a smoothed echo within a certain range of the expected bed level provides the most efficient approach. Level threshold methods do not enhance the bathymetry DEMs and echo gradient and curvature methods are less robust. Bed picking by cross-correlation with an echo model is more computationally expensive than the level threshold methods but it accounts for the shape of the complete bed echo rather than depending on a single value. Strictly speaking, the bed echo model approach is limited to flat seabeds and a perfectly horizontal sonar with a nadir beam normal to the bed, where only the grazing angle determines the incident angle between sonar lobe and bed. For rippled seabeds however, the exact morphology within the sonar footprint needs to be known a priori to adapt the echo shape to the true incident angle. Echo model methods may therefore rather serve as enhancement of the bathymetry computed by a threshold level method in a first run.

3.2 Hydrodynamics

Hydrodynamic data is displayed in Fig. 6. Over the tidal cycle, water depths range from 34 m at low tide to 37 m at hight tide. Current velocities measured by the lower ADV 0.12 m above the seabed range from 0.1 to 0.3 ms^{-1} . The depth averaged flow velocities measured by the downward-looking ADCP are 25% higher. Wave parameters were calculated using the velocity and

5   pressure data from the lower ADV. Significant wave heights range from below 0.5 m in the first half of the measurement up to 2.5 m in the second half with a peak period between 8 s and 10 s.

To relate the hydrodynamic forcing to sediment mobility, Shields parameters were computed for wave (θ_w) and current (θ_c) forcing and the critical Shields parameter (θ_{cr}) was computed for the given median grain size following Soulsby (1997) (Fig. 7a). For the first 18 hours of the deployment, supercritical conditions were observed only during peak flood and ebb

10   current. Supercritical wave-induced conditions are reached for a period of 4 hours starting around 15:00 local time on the second day, followed by supercritical current-induced conditions lasting for around 4 hours during flood current.

3.3 Ripple dimensions

Ripples with a wave length of $\lambda_{m,t} = 0.215$ m and a height of $\eta_{m,t} = 0.013$ m (aspect ratio $\psi = 0.06$) were detected in the bathymetry below the lander using the transect method (Fig. 7b,c). The dimensions remain stable for the first 24 hours of the

15   deployment and the bedforms are considered inactive during this period. The scatter of their measured dimensions is used to quantify the precision of the methods used for their detection. In coincidence with the increasing flood current velocities and wave action on the seafloor from 24 hours onwards, the ripple height decreases by 0.004 m over a period of 2 hours and increases to the initial height over the following 6 hours with increasing tidal current velocity. No significant changes in ripple wave length can be observed. In terms of height evolution the trend of change of ripple height on the second day of the

20   deployment is captured by all three methods. The statistical methods returns the most robust results resulting in less scatter between successive measurements.

Predicted current ripple dimensions using Eq. (6) and (7) from Soulsby et al. (2012) are constant due to the sole dependence on median grain size. They result in $\eta_{p,c} = 0.015$ m and $\lambda_{p,c} = 0.124$ m. Predicted wave ripple dimensions from Eq. (9) and (10) follow the evolution of wave orbital velocities, however waves are expected to be dominant only where $\theta_w > \theta_c$

25   (Fig. 7a: Day 2, 15:00 h – 19:00 h). During this period, the maximum predicted wave ripple dimensions are $\eta_{p,w} = 0.017$ m and $\lambda_{p,w} = 0.115$ m.

The largest bedform heights of 0.019 m are obtained by the statistical method followed by 0.016 m by the image extrema methods whereas the evaluation of extrema in individual grid transects yields the lowest absolute heights of 0.013 m (Fig. 8a). In comparison with predicted ripple height, all three methods fall within the range between mean (0.011 m) and maximum

30   (0.024 m) bedform height as given by Flemming (1988) (Fl88). The predicted height for wave (So12w) and current ripples (So12c) by Soulsby et al. (2012), 0.015 m and 0.016 m respectively, coincide best with the height measured using image extrema.

3.4 Hydraulic roughness

Roughness lengths $z_{0,f}$ and Nikuradse's equivalent sand roughness $k_{s,f}$ resulting from the different ripple heights and the length from the transect method are summarized in Tab. 2. Reduction factors with regard to the statistical method are also presented. Due to the squared ripple height in Eq. 12, the difference between the methods is more pronounced and results in a factor of two between the statistical method and the transect method.

4   Discussion

4.1   Methods for dimension measurement

Only one method is shown for the calculation of ripple orientation and length from the sonar data, but three methods can be compared for the calculation of ripple heights. The statistical method (e.g. Traykovski et al., 1999) assumes a two-dimensional sinusoidal ripple field and computes its root mean square height. The second method picking regional extrema in the bathymetry only measures the height of a limited number of features. The evaluation of transects makes use of the complete scan at the grid resolution and averages over a larger number of regional extrema along the transects.

If bedform dimensions are computed from transects perpendicular to bedform crests, the result depends on the lateral position of the transect. As can be seen in Fig. 1b, ripples found in the field often exhibit curved crest lines of limited length rather than being purely two-dimensional features. Furthermore, the instantaneously observed rippled seabed always holds a history of varying dominant forcing drivers, magnitudes and directions. Transitional states may comprise newly formed active ripples superimposed on decaying relict ripples with different orientation. Within a three-dimensional field, any selected transect will cut across individual ripples at an arbitrary position with respect to its lateral elevation profile. The ripple height can only be regarded as meaningful by statistically evaluating multiple transects. This is underlined by van der Mark et al. (2008), who state that bedforms are far from regular features that can be easily described using mean values, even in laboratory flume experiments with uniform sediment and stationary flow conditions.

4.2   Precision of measurement

To assess the *accuracy* of the measurement of an a priori known topography under controlled laboratory conditions would be required. This cannot be achieved under field conditions. However, the *precision* of the different methods described here, i.e., the repeatability of a dimension measurement, can be estimated from the inter-comparison of the different methods and the temporal variability of the dimensions obtained from each individual method during stationary, inactive periods.

The different methods for ripple height measurement yield different absolute values but the magnitude of the change in height is captured by all three methods. For a better assessment of the precision of the methods, bedform dimensions from the first 18 hours of the deployment were summarized in box plots exhibiting the distribution of ripple height and length during stationary conditions. The results shown in Fig. 8 indicate that both ripple height and wave length can be measured with a precision smaller than 10% of their absolute dimensions, regardless of the method used. The distributions of ripple height for

all three methods are negative-skewed. Judging from 25$^{\text{th}}$ and 75$^{\text{th}}$ percentiles, the statistical method provides the most narrow range of ripple height while image and transect extrema yield comparable ranges.

As for ripple length, both 2D cross-correlation and DFT did not prove robust and the transect method remains. Its results fall into the wide range of lengths predicted by Yalin (1985) but is around 60% larger than lengths predicted Soulsby et al. (2012) for wave ripples and still about 40% larger than length predicted for current ripples scaling with grain size only.

4.3 Form roughness

The overestimation of ripple height has a significant effect on the calculation of hydraulic roughness due to the fact that height is used in a power of two in common roughness predictors (see list in Lefebvre et al. (2011)). While the predicted heights are in good general agreement with measured values, the So12 predictor tends to represent maximum heights of individual ripples rather than an along-crest average height given a certain three-dimensionality with varying crest elevation. If ripple height measured as average over individual transects is compared to the results from the statistical method, it is found that the latter gives values 40% larger than the transect method. This corresponds to an increase of roughness height by a factor of 1.56 if the ripple dimensions are used to predict form roughness using bedform roughness height as given by Eq. (11) (van Rijn, 1984) and an increase of roughness height by a factor of 1.96 using the relation given by Eq. (12) (Soulsby, 1997).

5 Conclusions

A setup of instruments and data processing methods for field measurements of ripple dimensions and dynamics was described. While the *accuracy* of the measured ripple dimensions cannot be determined without an absolute reference value, both ripple heights and wave lengths can be measured with a *precision* smaller than 10% of their absolute dimensions during inactive conditions. All methods tested are consistent with regard to the ripple dimensions computed. Observed relative changes in height are in the order of several millimeters between successive scans during active periods. When sticking to one method the dynamics of ripple dimensions, i.e., the relative changes can be reliably obtained and linked to changes in the forcing hydrodynamics.

The overall range of current ripple height can be predicted using the empirical relation by Flemming (1988). The wave and current ripple predictors from Soulsby et al. (2012) fits measured heights more closely but this method returns maximum ripple heights rather than spatial averages. Measured ripple lengths fall in the wide range given by Yalin (1985) but are somewhat longer compared to lengths predicted for both wave (Soulsby et al., 2012) and current (Yalin, 1964; Soulsby et al., 2012) dominated ripples.

The performance of time-evolving predictors introduced by Traykovski (2007) and Soulsby et al. (2012) could not be evaluated. The predictor of Traykovski (2007) was developed for wave-orbital ripples in more energetic environments. Both predictors could not predict the small range of dynamic evolution of ripple heights in the field data. This may be related to the migration of the ripples due to nonlinear interaction of wave and current forcing.

The commonly used statistical estimation of ripple height yields ripple heights 40% larger than average heights obtained by the transect method. This results in calculated form roughness height to increase by a factor of two. To account for the spatial variability of ripple heights, dimensions derived from transects should be considered whenever spatial bathymetry data with sufficient resolution is available.

5 *Author contributions.* C. Winter designed the field campaign and measurement setup on the *SedObs* lander. K. Krämer and C. Winter collected the data during cruises HE441 and HE447 on board RV *Heincke* with support of the Coastal Dynamics group at MARUM. K. Krämer performed the data processing and analysis the data. K. Krämer and C. Winter wrote the manuscript.

Acknowledgements. This work has been supported through the Coastal Observing System for Northern and Arctic Seas (COSYNA). Data presented here was collected by the MARUM Coastal Dynamics group. Their willingness to suffer in heavy seas is gratefully acknowledged.
10 The authors also appreciate the support from captain and crew on RV *Heincke*. Processed hydrodynamic ADV data which was kindly provided by S.M. Amirshahi. K. Krämer appreciates the support of GLOMAR – Bremen International Graduate School for Marine Sciences.

References

Ahmerkamp, S., Winter, C., Janssen, F., Kuypers, M. M. M., and Holtappels, M.: The impact of bedform migration on benthic oxygen fluxes, J. Geophys. Res. Biogeosci., pp. 2229–2242, doi:10.1002/2015JG003106, 2015.

Amos, C. L. and Collins, M. B.: The combined effects of wave motion and tidal currents on the morphology of intertidal ripple marks; The Wash, U.K., Journal of Sedimentary Research, 48, 849–856, doi:10.1306/212F758B-2B24-11D7-8648000102C1865D, 1978.

Amos, C. L., Bowen, A. J., Huntley, D. A., and Lewis, C. F. M.: Ripple generation under the combined influences of waves and currents on the Canadian continental shelf, Continental Shelf Research, 8, 1129–1153, doi:10.1016/0278-4343(88)90016-7, 1988.

Bartholdy, J., Ernstsen, V. B., Flemming, B. W., Winter, C., Bartholomä, A., and Kroon, A.: On the formation of current ripples, Scientific Reports, 5, 11 390, doi:10.1038/srep11390, 2015.

Bell, P. and Thorne, P.: Application of a high resolution acoustic scanning system for imaging sea bed microtopography, in: Seventh International Conference on Electronic Engineering in Oceanography, 1997. Technology Transfer from Research to Industry, 1997.

Bell, P. S. and Thorne, P. D.: Field measurements of wave induced sand ripples in three dimensions, in: 2nd International Conference on Underwater Acoustic Measurements: Technologies & Results, 2007.

Clifton, H. E. and Dingler, J. R.: Wave-formed structures and paleoenvironmental reconstruction, Marine Geology, 60, 165–198, 1984.

Flemming, B.: Zur Klassifikation subaquatischer, strömungstransversaler Transportkörper, Bochumer geologische und geotechnische Arbeiten, 29, 1988.

Grant, W. D. and Madsen, O. S.: Combined wave and current interaction with a rough bottom, J. Geophys. Res., 84, 1797–1808, doi:10.1029/JC084iC04p01797, 1979.

Hay, A. E. and Mudge, T.: Principal bed states during SandyDuck97: Occurrence, spectral anisotropy, and the bed state storm cycle, J. Geophys. Res., 110, C03 013, doi:10.1029/2004JC002451, 2005.

Hay, A. E. and Wilson, D. J.: Rotary sidescan images of nearshore bedform evolution during a storm, Marine Geology, 119, 57–65, doi:10.1016/0025-3227(94)90140-6, 1994.

Janssen, F.: Pore-water advection and organic matter mineralization in North Sea shelf sands, Ph.D. thesis, University of Bremen, 2004.

Knaapen, M. A. F.: Sandwave migration predictor based on shape information, J. Geophys. Res., 110, F04S11, doi:10.1029/2004JF000195, 2005.

Lefebvre, A.: Bed roughness over vegetated beds, Ph.D. thesis, University of Southampton, 2009.

Lefebvre, A., Ernstsen, V. B., and Winter, C.: Influence of compound bedforms on hydraulic roughness in a tidal environment, Ocean Dynamics, 61, 2201–2210, doi:10.1007/s10236-011-0476-6, 2011.

Li, M. Z. and Amos, C. L.: Predicting ripple geometry and bed roughness under combined waves and currents in a continental shelf environment, Continental Shelf Research, 18, 941–970, doi:10.1016/S0278-4343(98)00034-X, 1998.

Maier, I. and Hay, A. E.: Occurrence and orientation of anorbital ripples in near-shore sands, J. Geophys. Res., 114, F04 022, doi:10.1029/2008JF001126, http://onlinelibrary.wiley.com/doi/10.1029/2008JF001126/abstract, 2009.

Malarkey, J., Baas, J. H., Hope, J. A., Aspden, R. J., Parsons, D. R., Peakall, J., Paterson, D. M., Schindler, R. J., Ye, L., Lichtman, I. D., Bass, S. J., Davies, A. G., Manning, A. J., and Thorne, P. D.: The pervasive role of biological cohesion in bedform development, Nat Commun, 6, doi:10.1038/ncomms7257, 2015.

Marine Electronics Ltd.: 3D Profiling Sonar - Model 2001 Datasheet, http://www.marine-electronics.co.uk/brochures/3DSonar/2001.pdf, accessed: 2015-03-23, 2004.

Nelson, T. R. and Voulgaris, G.: A spectral model for estimating temporal and spatial evolution of rippled seabeds, Ocean Dynamics, 65, 155–171, doi:10.1007/s10236-014-0801-y, 2014.

Nelson, T. R., Voulgaris, G., and Traykovski, P.: Predicting wave-induced ripple equilibrium geometry, J. Geophys. Res. Oceans, 118, 3202–3220, doi:10.1002/jgrc.20241, 2013.

5   Schindler, R. J., Parsons, D. R., Ye, L., Hope, J. A., Baas, J. H., Peakall, J., Manning, A. J., Aspden, R. J., Malarkey, J., Simmons, S., Paterson, D. M., Lichtman, I. D., Davies, A. G., Thorne, P. D., and Bass, S. J.: Sticky stuff: Redefining bedform prediction in modern and ancient environments, Geology, 43, 399–402, doi:10.1130/G36262.1, 2015.

Smyth, C. and Hay, A. E.: Wave Friction Factors in Nearshore Sands, J. Phys. Oceanogr., 32, 3490–3498, doi:10.1175/1520-0485(2002)032<3490:WFFINS>2.0.CO;2, 2002.

10   Smyth, C. E. and Li, M. Z.: Wave-current bedform scales, orientation, and migration on Sable Island Bank, J. Geophys. Res., 110, C02 023, doi:10.1029/2004JC002569, 2005.

Soulsby, R.: Dynamics of Marine Sands: A Manual for Practical Applications, Thomas Telford, 1997.

Soulsby, R. L. and Whitehouse, R. J. S.: Prediction of ripple properties in shelf seas - Mark 2 Predictor, 2005.

Soulsby, R. L., Whitehouse, R. J. S., and Marten, K. V.: Prediction of time-evolving sand ripples in shelf seas, Continental Shelf Research, 15   38, 47–62, doi:10.1016/j.csr.2012.02.016, 2012.

Traykovski, P.: Observations of wave orbital scale ripples and a nonequilibrium time-dependent model, J. Geophys. Res., 112, C06 026, doi:10.1029/2006JC003811, 2007.

Traykovski, P., Hay, A. E., Irish, J. D., and Lynch, J. F.: Geometry, migration, and evolution of wave orbital ripples at LEO-15, J. Geophys. Res., 104, 1505–1524, doi:10.1029/1998JC900026, 1999.

20   van der Mark, C. F., Blom, A., and Hulscher, S. J. M. H.: Quantification of variability in bedform geometry, J. Geophys. Res., 113, F03 020, doi:10.1029/2007JF000940, 2008.

van Rijn, L. C.: Sediment Transport, Part III: Bed forms and Alluvial Roughness, Journal of Hydraulic Engineering, 110, 1733–1754, doi:10.1061/(ASCE)0733-9429(1984)110:12(1733), 1984.

Venditti, J. G.: 9.10 Bedforms in Sand-Bedded Rivers, in: Treatise on Geomorphology, edited by Shroder, J. F., pp. 137–162, Academic 25   Press, San Diego, 2013.

Yalin, M.: On the Determination of Ripple Geometry, Journal of Hydraulic Engineering, 111, 1148–1155, doi:10.1061/(ASCE)0733-9429(1985)111:8(1148), 1985.

Yalin, M. S.: Geometrical properties of sand wave, Journal of the Hydraulics Division, 90, 105–119, 1964.

Zanke, U.: Grundlagen der Sedimentbewegung, Springer-Verlag, 1982.

Table 1. *SedObs* lander sensors, measured parameters and sampling rates.

Sensor	Parameter	Sampling rate
ADCP 1200 kHz (downward)	Flow velocity (profile) $\boldsymbol{u}(z)$	1 Hz
2×ADV	Flow velocity (point), Wave parameters	32 Hz
3D-ARP	Bathymetry $z(x,y)$	1 in 12 min.
CTD	Conductivity, temperature, pressure (C,T,P)	1 Hz
Digital camera	Underwater photos (first 90 min. of deployment only)	0.1 Hz

Table 2. Roughness lengths for measured ripple dimensions using Eq. (11) and (12).

Method	statistical	image extrema	transect
$z_{0,f}$ [m] Eq. (12)	0.00168	0.00119	0.00079
reduction with regard to stat. method	1.00	0.71	0.47
$k_{s,f}$ [-] Eq. (11)	0.01861	0.01486	0.01115
reduction with regard to stat. method	1.00	0.80	0.60
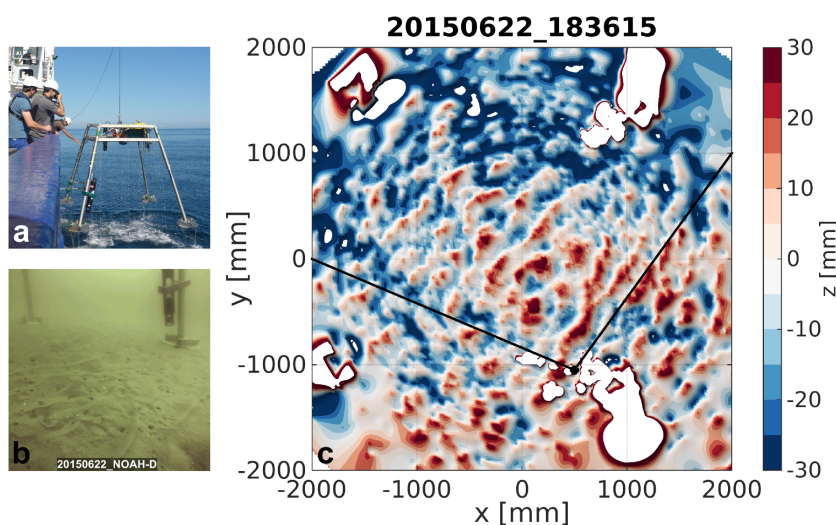
Figure 1. (a) Recovery of autonomous sea floor observatory *SedObs*. (b) Underwater photo showing rippled seabed. (c) Cropped sonar image with ripples and lander foot plates visible in the small scale bathymetry. Plane coordinates (x,y) are centered on sonar transducer and elevation z is given as zero-mean. The position and field of view of the camera in (b) are indicated by a black dot and black lines.
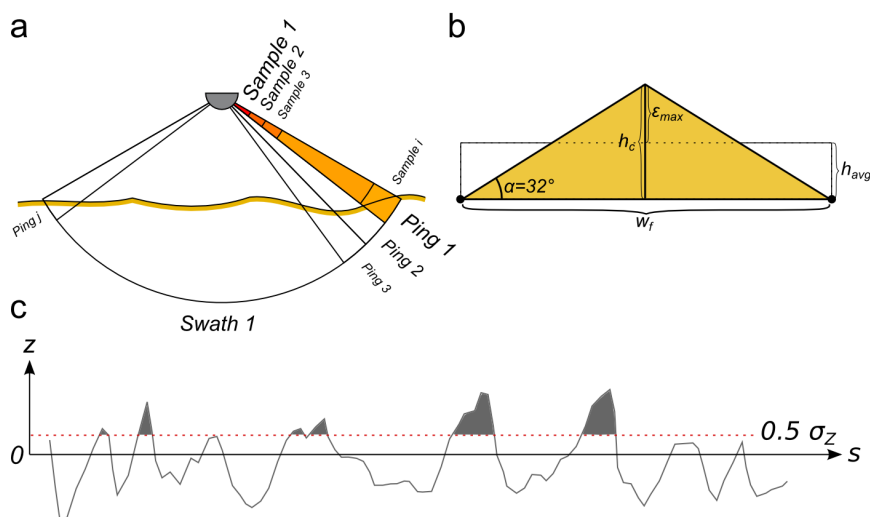
Figure 2. (a) Definitions of sonar samples, pings and swaths. (b) Estimation of maximum error in ripple crest height due to averaging over sonar footprint. (c) Generation of binary image from bathymetry using half the standard deviation of the elevation as cutoff threshold.
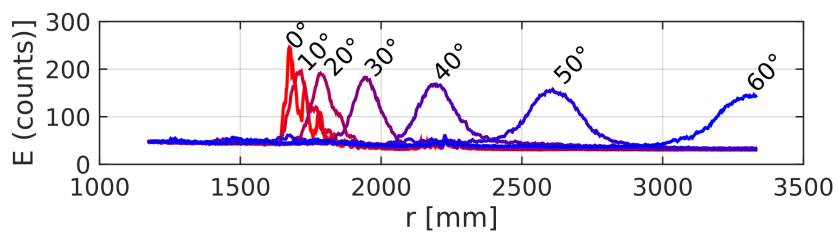
Figure 3. Echo intensities over range derived from scan averaged water column echoes for different grazing angles.
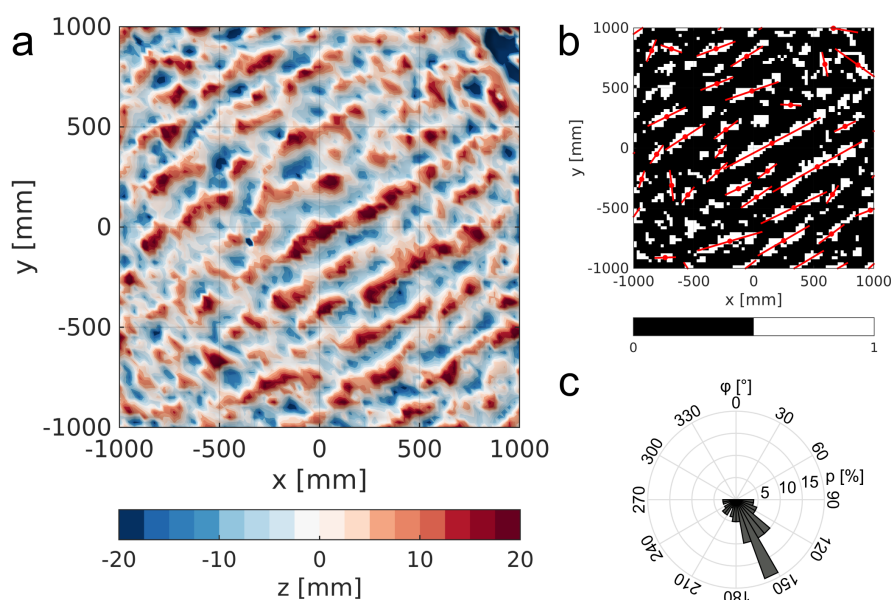
Figure 4. (a) Small scale bathymetry cropped to the central 2×2 m below the sonar. (b) Overlay of detected objects in 8-connected neighborhood on binary image with a threshold of $0.5\sigma_z$. Object centers and major axis are marked in red. (c) Polar histogram of ripple crest-perpendicular orientation in degrees from North with percentage of total number of objects on the radial axis.
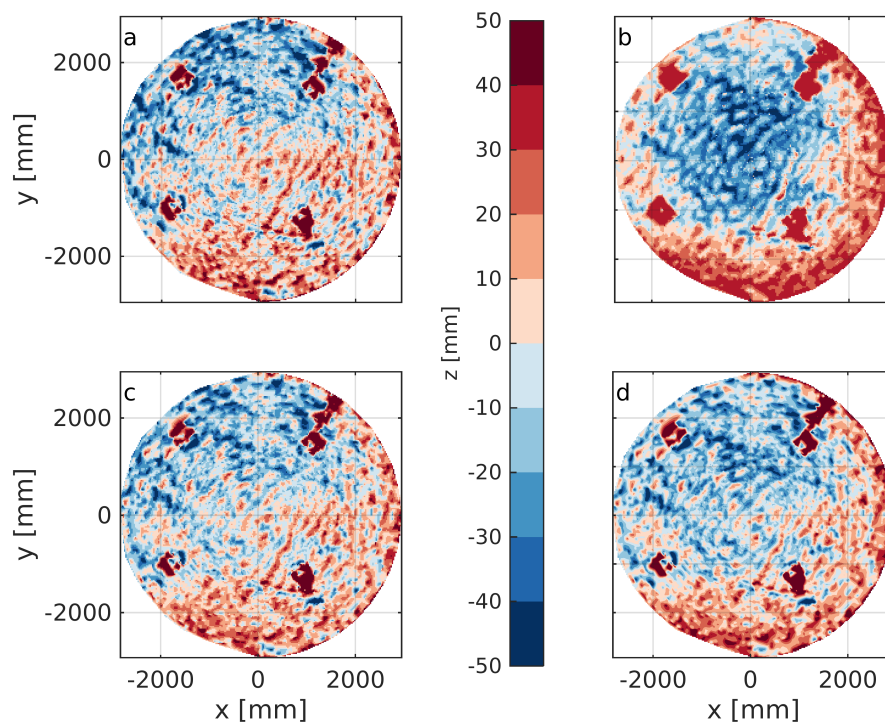
Figure 5. Comparison of bathymetries obtained from different bottom-picking methods. (a) Maximum echo, (b) 60% max. echo (Smyth and Li, 2005), (c) 80% max. echo (Lefebvre, 2009) and (d) grazing angle related coefficient of max. echo. Elevation z is given as zero-mean.
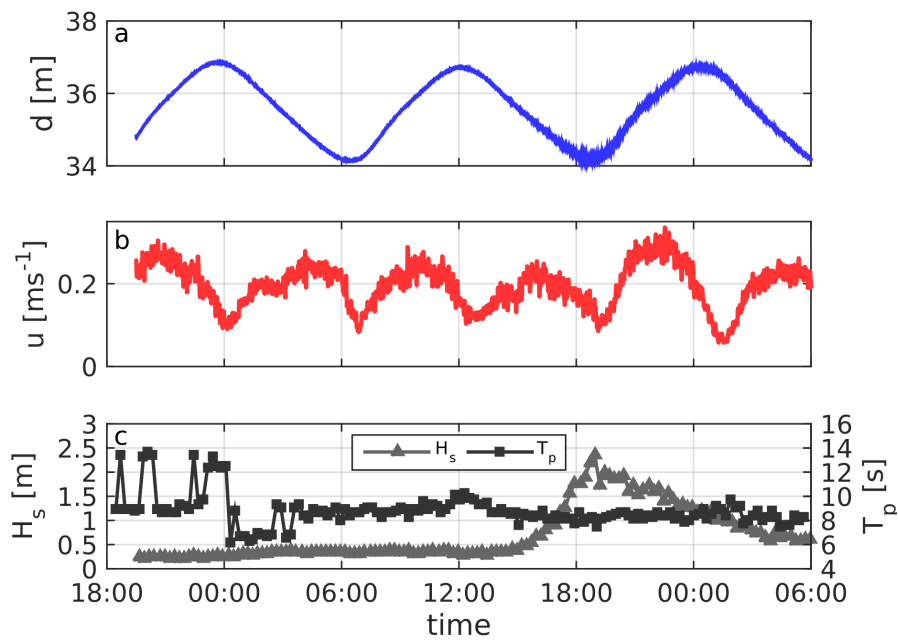
Figure 6. Hydrodynamic conditions at station NOAH-D, 20–22 March 2015. (a) Water level, (b) flow velocity at a height of 0.12 m above seafloor and (c) significant wave height and peak period.
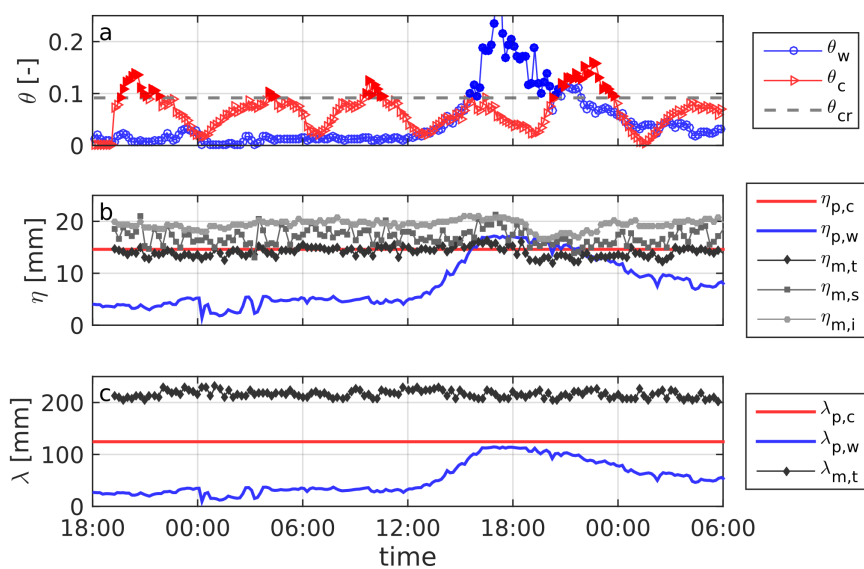
Figure 7. (a) Shields parameter for wave orbital velocities θ_w, tidal current θ_c and critical Shields parameter θ_{cr}. During supercritical conditions ($\theta > \theta_{cr}$), filled markers indicate the dominant forcing. (b) Evolution of ripple height and (c) wave length compared to predicted equilibrium dimension for wave and current forcing as given by Soulsby et al. (2012). Indices in the legends of (b) and (c) indicate: p-predicted, m-measured, c-current, w-wave, t-transect, s-statistical and i-image extrema.
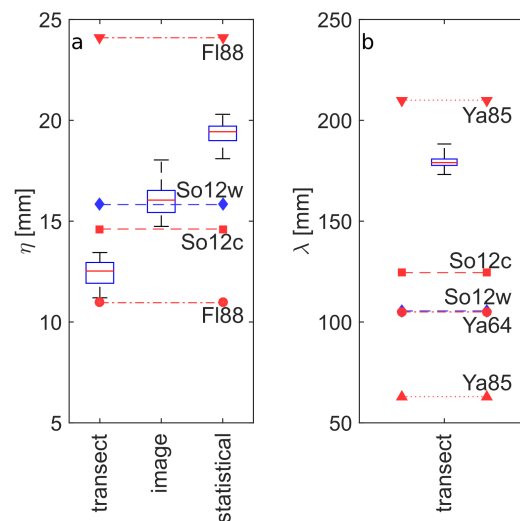
Figure 8. Box plots of the precision of measured dimensions during stationary conditions and accuracy in comparison with predicted equilibrium dimension for wave and current dominated conditions. (a) Bedform height, measured by 2D transect wise extrema, 3D image extrema and statistical method. Horizontal lines indicate predicted ripple height using the expressions from Soulsby et al. (2012) (So12w,c) and Flemming (1988) (Fl88). (b) Bedform wave length measured from 2D transects. Horizontal lines indicate predicted ripple length using the expressions from Soulsby et al. (2012) and Yalin (1964, 1985) (Ya64, Ya85). In box plots, red line denotes median, blue box indicates 25th and 75th percentiles and dashed lines extend to extreme values.